Hydropathicity-based prediction of pain-causing NaV1.7 variants

Makros N. Xenakis[a,b,*], Dimos Kapetis[c], Yang Yang[d,e], Monique M. Gerrits[f], Jordi Heijman[g], Stephen G. Waxman[h,i], Giuseppe Lauria[c,j], Catharina G. Faber[k], Ronald L. Westra[l], Patrick J. Lindsey[a,m], Hubert J. Smeets[a,b]

[a]*Department of Toxicogenomics, Section Clinical Genomics, Maastricht University, PO Box 616, 6200 MD Maastricht, the Netherlands*
[b]*Research School for Mental Health and Neuroscience (MHeNS), Maastricht University, PO Box 616, 6200 MD Maastricht, The Netherlands*
[c]*Neuroalgology Unit, Fondazione IRCCS Istituto Neurologico "Carlo Besta", via Celoria 11, 20133 Milan, Italy*
[d]*Department of Medicinal Chemistry and Molecular Pharmacology, Purdue University College of Pharmacy, West Lafayette, IN, 47907, USA*
[e]*Purdue Institute for Integrative Neuroscience, West Lafayette, IN 47907, USA*
[f]*Department of Clinical Genetics, Maastricht University Medical Center, PO box 5800, 6202 AZ, Maastricht, the Netherlands*
[g]*Department of Cardiology, CARIM School for Cardiovascular Diseases, Maastricht University, PO Box 616, 6200 MD Maastricht, The Netherlands*
[h]*Department of Neurology and Center for Neuroscience and Regeneration Research, Yale University School of Medicine, New Haven, CT 06510, USA.*
[i]*Rehabilitation Research Center, Veterans Affairs Connecticut Healthcare System, West Haven, CT 06516, USA.*
[j]*Department of Biomedical and Clinical Sciences "Luigi Sacco", University of Milan, via G.B. Grassi 74, 20157 Milan, Italy*
[k]*Department of Neurology, Maastricht University Medical Center, PO Box 5800, 6202 AZ Maastricht, The Netherlands*
[l]*Department of Data Science and Knowledge Engineering, Maastricht University, PO Box 616, 6200 MD Maastricht, the Netherlands*
[m]*Research School for Oncology and Developmental Biology (GROW), Maastricht University, PO Box 616, 6200 MD Maastricht, the Netherlands*

Abstract

Background: Mutation-induced variations in the functional architecture of the NaV1.7 channel protein are causally related to a broad spectrum of human pain disorders. Predicting *in silico* the phenotype of NaV1.7 variant is of major clinical importance; it can aid in reducing costs of *in vitro* pathophysiological characterization of NaV1.7 variants, as well as, in the design of drug agents for counteracting adhere pain symptoms.
Results: In this work, we utilize spatial complexity of hydropathic effects toward predicting which NaV1.7 variants cause pain (and which are neutral) based on the location of its mutation site within the NaV1.7 structure. For that, we

*Correspondence and requests for materials should be addressed to M.N.X. E-mail: mrksxenakis@gmail.com

analyze topological and scaling hydropathic characteristics of the atomic environment around NaV1.7's pore and probe their spatial correlation with mutation sites. We show that pain-related mutation sites occupy structural locations in proximity to a hydrophobic patch lining the pore while clustering at a critical hydropathic-interactions distance from the selectivity filter (SF). Taken together, these observations can differentiate pain-related NaV1.7 variants from neutral ones, i.e., NaV1.7 variants not causing pain disease, with 80.5% sensitivity and 93.7% specificity [area under the receiver operating characteristics curve = 0.872].

Conclusions: Our findings suggest that maintaining hydrophobic NaV1.7 interior intact, as well as, a finely-tuned (dictated by hydropathic interactions) distance from the SF might be necessary molecular conditions for physiological NaV1.7 functioning. The main advantage for using the presented predictive scheme is its negligible computational cost, as well as, hydropathicity-based biophysical rationalization.

Keywords:
NaV1.7, missense mutations, pain, atomic hydropathicity, computational modeling, cumulative hydropathic topology, scaling, pathogenicity prediction

---

Introduction

Voltage-gated sodium channels (NaVChs) are pore-forming proteins spanning the cell membrane. They are members of the ion channels superfamily and their main physiological role is to control transport of sodium ions across cell membranes. The human NaV1.7 channel is encoded by the *SCN9A* gene and is preferentially expressed in peripheral neurons (e.g., dorsal root ganglion (DRG) nociceptors) responsible for networking pain signals. The structure of the NaV1.7 α-subunits is that of a pore-forming tetramer via assembly of four heterogeneous domains (DI-DIV). Three intracellular loops (L1-L3) form structural interconnections among subsequent domains. Each domain comprises six transmembrane helices (S1-S6) organized into a pore module (PM) forming an ion-conduction pathway coupled with a voltage-senor (VS). Mechanistic description of NaV1.7's function is that VSs react to extracellular changes in ionic concentrations by moving outwards thus exerting a pulling force upon the PM which opens the channel pore. Closed-to-open gating transition leads to channel activation, i.e., renders it conductive to sodium ions. Missense mutations in the *SCN9A* gene can destabilize the NaV1.7's functional architecture thus disrupting physiological gating and, consequently, deregulate flow of sodium ions through the pore. At a cellular level, these genetically-caused destabilizations can affect neuronal excitability by inducing a gain-of-function (GOF) effect, i.e., by increasing the net ionic flow, thus triggering a wide spectrum of pain diseases such as inherited erythromelalgia (IEM) [1, 2, 3, 4, 5, 6, 7, 8, 9, 10, 11, 12, 13, 14, 15, 16, 17, 18, 19, 20, 21, 22, 23, 24, 25, 26, 27, 28, 29, 30, 31], paroxysmal extreme pain disorder (PEPD) [32, 33, 34, 35, 36, 37, 38, 39] and small fiber

neuropathy (SFN) [40, 41, 42, 43, 44]. A proof of concept for the GOF-pain correlation hypothesis came from identification of missense *SCN9A*-gene mutations inducing a loss-of-function (LOF) effect, i.e., decreasing sodium-ions membrane currents, that is causally related to clinical symptoms of loss of pain sensation [45, 46, 47].

Hydropathic interactions (HIs) represent a summary of fundamental molecular interactions [48] driving molecular phenomena such as protein folding, protein hydrophobic-core stability, self-assembly of amphiphilic molecules and "dewetting" transitions occurring at the nanoscale (for a review in HIs-driven phenomena see [49]). Within the field of ion channels research, experimental and computational studies have shown that HIs are crucial regulators of gating processes occurring within the pore's microenvironment (termed as hydrophobic gating phenomena [50]), as well as, of channel stability via formation of hydrogen bonds networks [51, 52] initiated by pore-lining hydrophobic residue patches [53]. Computational modeling of HIs combined with biophysical observations extracted from *in vitro* NaVCh pathophysiological characterization can propel our understanding of mechanistic linkages between mutation-induced perturbations and human pain pathophysiology. Key-studies toward this direction were these of Lampert et al [54] and of Yang et al [55] demonstrating how the F1449V mutation and the in-frame-deletion L955Del, respectively, can disrupt a hydrophobic ring stabilizing the putative activation gate (AG) of the NaV1.7 thus acting as disease-causing molecular triggers. Moreover, computational modeling successfully deduced an energetic coupling between two different IEM-related mutations foreseen by their geometrical proximity in NaV1.7 structure [7]. A question that naturally arose from these studies was whether a detailed examination of HIs network characteristics within a NaV1.7 structure can reveal statistically-significant but also biophysically-relevant differentiations among the WT structure and its variants. This question was probed by Kapetis et al [56]; a network-theoretical computational framework was introduced in order to capture changes in inter-atomic HIs within a NaV1.7 WT structure induced by pain-related mutations. The study reported on a betweenness centrality network measure achieving a statistically-important differentiation of pain-related variants from a collection of neutrals, i.e., variants not causing pain disease. Notably, this approach highlighted the prominent role that HIs play in NaV1.7's stability and reported on plausible mutation-mechanism scenarios disrupting hydrophobic contacts among neighboring and distant residues. Another remark on the multi-scale nature of HIs was made by the authors of [57] suggesting that a pathogenic mutation in the $KCNA1$ gene encoding the human voltage-gated potassium channel KV1.1 can de-tune HIs equilibrium (and, consequently, destabilize KV1.1's pre-open conformation) implying that mutation-induced perturbation effects can destroy finely-tuned network-like HIs expanding throughout the structure as a whole. Interestingly, the fine-tuning hypothesis was proposed also for the NaV1.7; a recent study employing a machine learning (MLE) computational pipeline for predicting NaV1.7's variant pathogenicity suggested that the fine-tuning of the NaV1.7 channel is so delicate that limits classification accuracy of practically any computational ap-

proach [97]. Taken together, these observations highlight the highly-cooperative nature of HIs [48] and suggest that even small changes in the hydropathic spatial distribution profile of a channel structure can have a detrimental impact on the functional architecture which, in turn, might induce clinically-observed alterations of electrophysiology.

Following [56, 97], this study aims at probing the finely-tuned hypothesis for the NaV1.7's atomic hydropathic environment in order to predict whether a NaV1.7 variant causes pain or not. We utilize a closed-state structural model of the NaV1.7 retrieved from homology modeling based on the pre-open NaVAb [58] template (first presented in [55] and later used also in [7]) and investigate cumulative, i.e., scale-dependent, hydropathic properties of its porous atomic environment in relation to structural locations of missense *SCN9A*-gene mutations. In order to tackle spatial complexities emerging from the highly-cooperative nature of HIs we adopt a modeling approach rooted in the hypothesis that proteins can be represented as self-organized criticality (SOC) [59] archetypes; protein structures are thought to have been evolutionary optimized with respect to extrema in some thermodynamic property (or properties) capturing a qualitative reorganization of the atomic environment [60, 61]. The intra-channel locations where these macroscopic thermodynamic changes take place correspond to so-called critical points of the atomic structure [60, 61]. The highly-cooperative nature of HIs has placed structure-retrieved hydropathic properties in the epicenter of SOC hypothesis [60, 61, 62, 63]). It is important to note that computational evidence for a universal hydrophobic-to-hydrophilic (or inside-outside with "inside" referring to the hydrophobic core and "outside" referring to the hydrophilic exterior) spatial transition in protein systems was first provided before the formulation of the SOC hypothesis (see [64]). Departing from this phenomenological basis, we here utilize the finite-size scaling analysis methodologies presented in [65, 66] for screening hydropathic morphology around NaV1.7's pore [65] toward identification of critical points associated with NaV1.7's functional architecture. Biophysical relevance of retrieved observations is justified not only in terms of the scale-invariance of a carefully-chosen cumulative hydropathicity-property function but also with respect to conserved structural NaV1.7 features such as the PM-VSs spatial transition and the location of the selectivity filter (SF). In particular, we demonstrate that the atomic cumulative distribution function around NaV1.7's pore exhibits a sigmoid profile with inflection points matching closely the conserved PM-VSs spatial transition. This provides a rigor description of atom-packing geometry and, consequently, a macroscopic partitioning of the atomic environment around the pore allowing for mapping the spatial profile of the atomic cumulative hydropathicity-property function and mutation sites on two dimensions. The SOC hypothesis is then accepted (or rejected) depending on whether the cumulative hydropathicity-property function is globally maximized and exhibits power-law-like scaling behavior in the vicinity of the inflection point (or not).

Our mapping procedures reveal the formation of a hydrophobic patch (HP) incorporating NaV1.7's central cavity (CC) and activation gate (AG). We report on two "hot" map areas attracting pain-related mutation sites which are dis-

tributed either inside or along HP's periphery. Probing the SOC hypothesis for the NaV1.7 structure reveals that "hot" structural locations tend to cluster at a distance of 33.4 Å from the SF. Stability implications of these observations can be concertized by considering that in the vicinity of the critical point the range and intensity of HIs increase in a power-law fashion thus favoring amplification and propagation of mutation-induced perturbations only peripherally to the HP and at critical HIs-distance from the SF thus not directly affecting neither of them. The clinical translational value of our findings is tested by predicting pathogenicity of 84 NaV1.7 variants; a weighted average of HP- and SF-related distance metrics can classify up to 29 (out of 36) pain-related variants and 45 (out of 48) neutral variants correctly.

Methods

All computations were performed in R [67] environment unless stated differently.

3D structure preparation

We fetch the NaV1.7 atomic structure model constructed via homology modeling procedures based on the pre-open NaVAb [58] template (for model construction details see [7]). Its principal axes were estimated by using the VMD software [68]. A global coordinate system $(\hat{\mathbf{x}}, \hat{\mathbf{y}}, \hat{\mathbf{z}})$ was introduced with its center at O and the NaV1.7's principal pore axis, i.e., the axis approximating the direction of the channel's pore, was aligned with the z-axis with orientation from the extracellular side (ES) toward the intracellular side (IS) with respect to $\hat{\mathbf{z}}$. The atomic center $\mathbf{e} = \frac{1}{M}\sum_{i=1}^{N_c} m_i \cdot \mathbf{c}_i$ of the 3D structure was set to overlap with O, where $\mathbf{c}_i = (\mathrm{c}_{x,i}, \mathrm{c}_{y,i}, \mathrm{c}_{z,i})$ is the atomic center of the i-th atom, m_i is the mass of the i-th atom, $N_c = 18567$ is the total number of atoms and $M = \sum_{i=1}^{N_c} m_i$ is the total molecular mass (values of atomic masses are the same as [**? ?**]).

Geometrical characteristics of the pore

We navigated through the skewed NaV1.7's pore by introducing pore points $\mathbf{p}$ (see Supplementary Material (SM), S1). The pore radius at $\mathbf{p}$ is given by [72]

$$R(\mathbf{p}) = \underset{i=1,2,..,N_c}{min} \{||\mathbf{c}_i - \mathbf{p}|| - vdW_i\} \tag{m2}$$

where $||\cdot||$ is the euclidean norm and vdW_i is the van der Waals radius of the i-th atom (values of van der Waals radii are the same as [**? ?**]). The distance between $\mathbf{p}$ and its nearest neighbor atom corresponds then to

$$D(\mathbf{p}) = \underset{i=1,2,..,N_c}{min} \{||\mathbf{c}_i - \mathbf{p}||\} \tag{m3}$$

and the outer surface radius at $\mathbf{p}$ is given by [65, 66]

$$L(\mathbf{p}) = \underset{i=1,2,..,N_c}{max} \{||\mathbf{c}_i - \mathbf{p}|| + vdW_i\} \tag{m4}$$

where the unit of measurement for $R(\mathbf{p})$, $D(\mathbf{p})$ and $L(\mathbf{p})$ is expressed in [Å].

Finite-size sampling around the pore

The atomic environment around $\mathbf{p}$ is sampled with concentric spheres placed at $\mathbf{p}$ of increasing radius [65, 66]

$$l_\alpha(\mathbf{p}) = D(\mathbf{p}) + \alpha \cdot \frac{L(\mathbf{p}) - D(\mathbf{p})}{K_\alpha} \text{ for } \alpha = 1, 2, .., K_\alpha \to \infty \tag{m5}$$

where K_α is the total number of sampling spheres and α denotes the index of the sampling sphere. $l_\alpha(\mathbf{p})$ indicates the size, i.e., molecular scale, of the spherical cluster of atoms around $\mathbf{p}$ in [Å] and $L(\mathbf{p})$ the finite channel size measured with respect to $\mathbf{p}$. Accordingly, the atomic cumulative distribution function (CDF) at $\mathbf{p}$ is given by [65, 66]

$$N(\mathbf{p}, l_\alpha(\mathbf{p})) = \sum_{i=1}^{N_c} \theta(l_\alpha(\mathbf{p}) - ||\mathbf{c}_i - \mathbf{p}||) \tag{m6}$$

where $\theta(\cdot)$ is the heaviside function. Note that $N(\mathbf{p}, l_\alpha(\mathbf{p}))$ essentially describes how atoms are packed around $\mathbf{p}$. In computational practice K_α is set to be "large enough" approximating the continuous case via dense sampling.

Mathematical modeling of atomic accumulation

Modeling of the CDF was performed by employing the GROFIT routine [73]. A collection of candidate models including re-parametrized algebraic forms [74] of the Logistic model [75]

$$n_{LOG}(\mathbf{p}, l_\alpha(\mathbf{p})) = A(\mathbf{p}) \cdot \big\{1 + \exp\big(\frac{4 \cdot t(\mathbf{p})}{A(\mathbf{p})} \cdot \big(s(\mathbf{p}) - l_\alpha(\mathbf{p})) + 2\big)\big\}^{-1} \tag{m7}$$

, of the Gompertz model [76]

$$n_{GOM}(\mathbf{p}, l_\alpha(\mathbf{p})) = A(\mathbf{p}) \cdot \exp\big(-\exp(\frac{e \cdot t(\mathbf{p})}{A(\mathbf{p})} \cdot (s(\mathbf{p}) - l_\alpha(\mathbf{p})) + 1)\big) \tag{m8}$$

with $e = \exp(1)$, of the the modified Gompertz model [77]

$$\begin{aligned} n_{MGOM}(\mathbf{p}, l_\alpha(\mathbf{p})) = & A(\mathbf{p}) \cdot \exp\big(-\exp\big(\frac{e \cdot t(\mathbf{p})}{A(\mathbf{p})} \cdot (s(\mathbf{p}) - l_\alpha(\mathbf{p})) + 1\big)\big) \\ & + A(\mathbf{p}) \cdot \exp\big(w(\mathbf{p}) \cdot (l_\alpha(\mathbf{p}) - l_{shift}(\mathbf{p}))\big) \end{aligned} \tag{m9}$$

and of the Richards model [78]

$$\begin{aligned} & n_{RIC}(\mathbf{p}, l_\alpha(\mathbf{p})) = A(\mathbf{p}) \cdot \big\{1 + \tilde{q}(\mathbf{p}) \cdot b(\mathbf{p}) \cdot \exp\big(-k(\mathbf{p}) \cdot l_\alpha(\mathbf{p})\big)\big\}^{-1/\tilde{q}(\mathbf{p})} \\ & \text{with } b(\mathbf{p}) = \exp\big(1 + \tilde{q}(\mathbf{p}) + k(\mathbf{p}) \cdot s(\mathbf{p})\big) \text{ and } k(\mathbf{p}) = \frac{t(\mathbf{p})}{A(\mathbf{p})} \cdot (1 + \tilde{q}(\mathbf{p}))^{1+1/\tilde{q}(\mathbf{p})} \end{aligned} \tag{m10}$$

were fitted on $N(\mathbf{p}, l_\alpha(\mathbf{p}))$ along $l_\alpha(\mathbf{p})$-direction where $\{A(\mathbf{p}), t(\mathbf{p}), s(\mathbf{p}), \tilde{q}(\mathbf{p}), w(\mathbf{p}), l_{shift}(\mathbf{p})\}$ are model parameters. The mathematical model that best fitted $N(\mathbf{p}, l_\alpha(\mathbf{p}))$

traces along $l_\alpha(\mathbf{p})$-direction was selected based on minimization of an Akaike information criterion (see [73] for algorithmic details).

Following [66], model parameters interpretation was performed with respect to the inflection point

$$\xi(\mathbf{p}) = \{l_\alpha(\mathbf{p}) \mid \frac{\partial^2 n(\mathbf{p}, l_\alpha(\mathbf{p}))}{\partial l_\alpha(\mathbf{p})^2} = 0\} \tag{m11}$$

that determines the location along $l_\alpha(\mathbf{p})$-direction where the radial distribution function (RDF), $\frac{\partial n(\mathbf{p}, l_\alpha(\mathbf{p}))}{\partial l_\alpha(\mathbf{p})}$, maximizes. The RDF maximum value is given by the parameter $t(\mathbf{p})$ accounting for the maximum atomic accumulation rate (or, equivalently, for the maximum atomic density) around $\mathbf{p}$. Parameter $A(\mathbf{p})$ is the asymptote value of the fitted model, i.e., $n(\mathbf{p}, l_\alpha(\mathbf{p}) \to \infty) = A(\mathbf{p})$, describing what happens when $L(\mathbf{p})$ becomes arbitrary large. Parameter $s(\mathbf{p})$ determines the location along $l_\alpha(\mathbf{p})$-direction where the lag domain ends, i.e., the size of the lag atomic accumulation domain. Interpretation of parameter $t(\mathbf{p})$ is retrieved in terms of the ratio $t(\mathbf{p}) = \frac{A(\mathbf{p})}{os(\mathbf{p}) = o(\mathbf{p}) - s(\mathbf{p})}$ with $o(\mathbf{p})$ determining the location along $l_\alpha(\mathbf{p})$-direction where the asymptote atomic accumulation domain begins. Parameter $\tilde{q}(\mathbf{p})$ affects the shape of the Richards model curve, as well as, the location of the inflection point along $l_\alpha(\mathbf{p})$-direction thus plays the role of the summary atom-packing parameter. Parameters $w(\mathbf{p})$ and $l_{shift}(\mathbf{p})$ of the modified Gompertz model indicate the location and the slope, respectively, of a second increase in the modified Gompertz model curve (see [73]). The Logistic and the Gompertz model are retrieved from the Richards model for $\tilde{q}(\mathbf{p}) = 1$ and $\tilde{q}(\mathbf{p}) \to 0$, respectively, as shown in [79], thus they are considered as special cases of the Richards model.

Cumulative hydropathicity-property functions

The hydropathic density of the atomic environment around $\mathbf{p}$ was approximated in terms of [65]

$$\begin{aligned} m^{(0)}(\mathbf{p}, l_\alpha(\mathbf{p})) &= \frac{h^{(0)}(\mathbf{p}, l_\alpha(\mathbf{p}))}{N(\mathbf{p}, l_\alpha(\mathbf{p}))} \sim kcal/(mol \equiv atom) \\ \text{with } h^{(0)}(\mathbf{p}, l_\alpha(\mathbf{p})) &= \sum_{i=1}^{N_c} \theta(l_\alpha(\mathbf{p}) - ||\mathbf{c}_i - \mathbf{p}||) \cdot HI_i^w \end{aligned} \tag{m12}$$

where $\boldsymbol{h}^{(0)}(\mathbf{p}, l_\alpha(\mathbf{p}))$ corresponds to the cumulative zero-order hydropathic pore moment function [80] with $HI_i^w = HI_i + w_i$ representing the i-th atomic hydrophobic index in accordance with the corrected Kapcha-Rossky atomic hydrophobic scale presented in [65] (note that the Kapcha-Rossky atomic hydrophobic scale was initially published in [81] where a HIS atom was missing and was later added in [65]) with additive gaussian noise $w_i \in \mathcal{N}(\mu = 0, \sigma = 0.001)$. The superscript "(0)" indicates the moment order.

The hydropathic inter-atomic interaction strength (HIIS) at $\mathbf{p}$, i.e., the average interaction strength between an atomic component found within the cluster

of size $N(\mathbf{p}, l_\alpha(\mathbf{p}))$ and its surroundings, was approximated in terms of the hydropathic imbalance (or interaction strength) pore function [65, 66]

$$\begin{aligned}
\vec{\boldsymbol{m}}^{(1)}(\mathbf{p}, l_\alpha(\mathbf{p})) &= \frac{\vec{\boldsymbol{h}}^{(1)}(\mathbf{p}, l_\alpha(\mathbf{p}))}{N(\mathbf{p}, l_\alpha(\mathbf{p}))} \sim kcal\cdot\text{Å}/(mol\equiv atom) \\
\text{with } \vec{\boldsymbol{h}}^{(1)}(\mathbf{p}, l_\alpha(\mathbf{p})) &= \sum_{i=1}^{N_c} \theta(l_\alpha(\mathbf{p}) - ||\mathbf{c}_i - \mathbf{p}||)\cdot HI_i^w \cdot \vec{\boldsymbol{r}}_{\mathrm{p},i} \\
&= \underbrace{h_x^{(1)}(\mathbf{p}, l_\alpha(\mathbf{p}))\cdot\hat{\mathbf{x}} + h_y^{(1)}(\mathbf{p}, l_\alpha(\mathbf{p}))\cdot\hat{\mathbf{y}}}_{\vec{\boldsymbol{h}}_{xy}^{(1)}(\mathbf{p}, l_\alpha(\mathbf{p}))} + \underbrace{h_z^{(1)}(\mathbf{p}, l_\alpha(\mathbf{p}))\cdot\hat{\mathbf{z}}}_{\vec{\boldsymbol{h}}_z^{(1)}(\mathbf{p}, l_\alpha(\mathbf{p}))}
\end{aligned} \tag{m13}$$

where $\vec{\boldsymbol{h}}^{(1)}(\mathbf{p}, l_\alpha(\mathbf{p}))$ corresponds to cumulative first-order hydropathic pore moment function [80] quantifying the hydropathic inter-cluster interaction strength (HIcIS) with $\vec{\boldsymbol{r}}_{\mathrm{p},i}$ being the vector from $\mathbf{p}$ to $\mathbf{c}_i$. The superscript "(1)" indicates the moment order.

Introduction of the weak noise source w_i practically guarantees that $|h^{(0)}(\mathbf{p}, l_\alpha(\mathbf{p}))|$ and $||\vec{\boldsymbol{h}}^{(1)}(\mathbf{p}, l_\alpha(\mathbf{p}))||$ are non-zero for every combination of $\mathbf{p}$ and $l_\alpha(\mathbf{p})$ while their scaling behavior remains practically unaffected. Throughout this study we consider pore's physichochemical field characteristics to be adequate described in terms of the axial component, $\vec{\boldsymbol{m}}_z^{(1)}(\mathbf{p}, l_\alpha(\mathbf{p})) = \vec{\boldsymbol{h}}_z^{(1)}(\mathbf{p}, l_\alpha(\mathbf{p}))/N(\mathbf{p}, l_\alpha(\mathbf{p})) = m_z^{(1)}(\mathbf{p}, l_\alpha(\mathbf{p}))\cdot\hat{\mathbf{z}}$ given that the magnitude of the radial component, $||\vec{\boldsymbol{m}}_{xy}^{(1)}(\mathbf{p}, l_\alpha(\mathbf{p}))|| = ||\vec{\boldsymbol{h}}_{xy}^{(1)}(\mathbf{p}, l_\alpha(\mathbf{p}))||/N(\mathbf{p}, l_\alpha(\mathbf{p}))$, is vanishingly small relative to $||\vec{\boldsymbol{m}}^{(1)}(\mathbf{p}, l_\alpha(\mathbf{p}))||$ after a cut-off, lag-domain scale (see SM, S2). Hence, we focus throughout this study only on the scaling behavior and topology of the HIIS axial field component which can occupy only two states; an "in" state which is characterized by $\vec{\boldsymbol{m}}_z^{(1)}(\mathbf{p}, l_\alpha(\mathbf{p}))$ pointing towards the intracellular side (IS), i.e., by $m_z^{(1)}(\mathbf{p}, l_\alpha(\mathbf{p})) > 0$, and an "out" state which is characterized by $\vec{\boldsymbol{m}}_z^{(1)}(\mathbf{p}, l_\alpha(\mathbf{p}))$ pointing towards the extracellular side (ES), i.e., by $m_z^{(1)}(\mathbf{p}, l_\alpha(\mathbf{p})) < 0$. Topological changes in HIIS axial field component are detected according to the algorithmic scheme presented in [65] (see SM, S3).

Finite-size scaling of HIIS

In accordance to [66], a scale-invariant interval of the HIIS axial component corresponds to combinations of $\mathbf{p}$ with α for which the power-law approximation

$$||\vec{\boldsymbol{m}}_z^{(1)}(\mathbf{p}, l_\alpha(\mathbf{p}))|| \sim l_\alpha(\mathbf{p})^{\gamma(\mathbf{p})} \tag{m14}$$

is accurately satisfied indicating that HIIS stabilizing the cluster of $N(\mathbf{p}, l_\alpha(\mathbf{p}))$ atoms around $\mathbf{p}$ span a range up to $\sim l_\alpha(\mathbf{p})$ Å. Sign of $\gamma(\mathbf{p})$ quantifies the rate at which intensity and range of HIIS increase or decrease for increasing atomic cluster size. From a HIs-network standpoint, $\gamma(\mathbf{p})$ indicates whether HIs network interconnectivity is up- or down-regulated, i.e., whether HIs bonds, e.g., hydrogen bonds, are created or destroyed within the structure. The energy levels

associated with HIs bonds formation (or de-formation) guaranteeing stability of the atomic cluster can then be approximated by

$$U(\mathbf{p}, l_\alpha(\mathbf{p})) := ||\vec{\boldsymbol{h}}_z^{(1)}(\mathbf{p}, l_\alpha(\mathbf{p}))||/l_\alpha(\mathbf{p}) \sim N(\mathbf{p}, l_\alpha(\mathbf{p})) \cdot l_\alpha(\mathbf{p})^{\gamma(\mathbf{p})-1} \qquad \text{(m15)}$$

measured in kcal/(mol≡atomic cluster).

Results

In Figure 1 we demonstrate that atomic accumulation around NaV1.7's pore follows a sigmoid profile which can be accurately described by the Richards model (SM, S4). Inflection behavior of atomic accumulation can thus be described in terms of the inflection points, $\xi(\mathbf{p})$, so that the atomic environment around the pore is partitioned into four consecutive domains spanning NaV1.7 from the inside to the outside (Figure 1(b),(c)). Structural locations of the inflection points correspond to intra-channel regions where the atomic density maximizes and were found to closely follow the PMs-VSs spatial transition (see SM, S5 for calculation of PMs-VSs spatial transition characteristics). Accordingly, $\xi(\mathbf{p})$ serves as a macroscopic boundary line splitting the atomic environment around NaV1.7's pore into two phases, namely, a pre-inflection phase for $l_\alpha(\mathbf{p}) \leq \xi(\mathbf{p})$ and a post-inflection phase for $l_\alpha(\mathbf{p}) > \xi(\mathbf{p})$ accounting for atomic sub-environments containing mainly structural components belonging to the PMs and VSs, respectively (Figure 1(b)).

Based on the geometrical partition scheme summarized in Figure 1 we proceeded with mapping of missense *SCN9A*-gene mutation intra-channel structural locations. For that, we utilized a set of well-studied GOF NaV1.7 mutations prototypically related with IEM, SFN and PEPD pain disease (total number of pain-related mutation sites: 36) and a set of neutral NaV1.7 mutations, i.e., NaV1.7 variants not causing disease, (total number of neutral mutations: 48) and retrieved their corresponding two-dimensional map site (SM, S7).

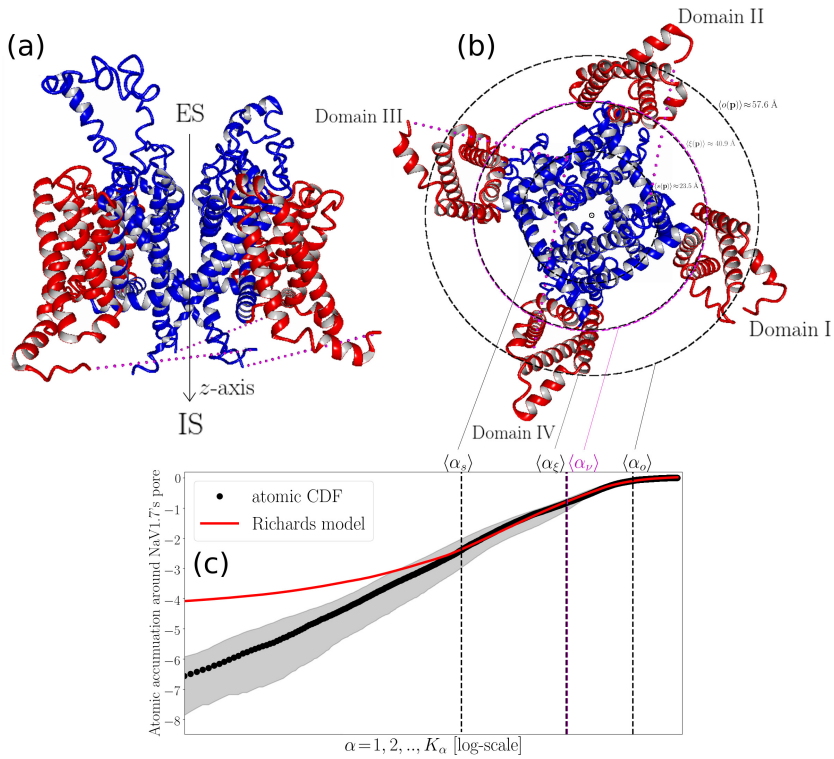

Figure 1: ***Atomic accumulation around NaV1.7's pore.*** *(a),(b) Cartoon illustration of the NaV1.7 human channel (side and top views). The atomic environment around the pore is partitioned into three consecutive domains; a lag domain, an inflection domain, and an asymptote domain. The upper boundaries of the lag domain, of the pre-inflection domain and of the post-inflection domain are also shown in terms of their statistical representations* $\langle\alpha_s\rangle$, $\langle\alpha_\xi\rangle$, $\langle\alpha_\xi\rangle \approx \langle\alpha_\nu\rangle$ *and* $\langle\alpha_o\rangle$, *respectively. Helical structures in (a),(b) forming the PMs and the VSs are colored with red and blue color, respectively. (c), Traces of statistical representations of the normalized (with respect to* N_c*) atomic CDF,* $\langle\bar{N}(\mathbf{p}, l_\alpha(\mathbf{p}))\rangle_\alpha$, *and of its best-fitted Richards model* $\langle n(\mathbf{p}, l_\alpha(\mathbf{p}))\rangle_\alpha$ *are plotted in log-scale with shaded areas around* $\langle N(\mathbf{p}, l_\alpha(\mathbf{p}))\rangle_\alpha$ *indicative of 95% confidence intervals. Statistical representations of scalars are calculated according to SM, S6.*

The majority (i.e., 54%) of pain-related mutations sites are sparsely distributed within the inflection domain attracted and, more precisely, attracted toward a centrally-located map area in the vicinity of the inflection-points line α_ξ (see area II on Figure 2(a) in relation to Figures 2(b),(c)). On the other hand, the majority (i.e., 75%) of neutral mutation sites are distributed within the second part of the inflection domain so their map density tends to maximize approximately in the middle of the second part of the inflection domain (see area III on Figure 2(a) in relation to Figures 2(b),(c)). The rest 46% of pain-related mutation sites are found within the lag domain toward the intracellular side of

the NaV1.7. In particular, their map density maximizes in the vicinity of the boundary line α_s toward the IS (see area I on Figure 2(a) in relation to Figures 2(b),(c)). Taken together, these observations indicate that for decreasing molecular scale the probability of a missense *SCN9A*-gene mutation to translate into a pain-related phenotype increases which is of little surprise considering that mutations affecting NaV1.7's interior are more likely to perturb packing of S5-S6 pore-forming helices and, consequently, affect pore's gating behavior.

Mapping of hydropathic density profile reveals the formation of a large HP incorporating the central cavity (CC) and the AG (Figure 3). Specifically, we demonstrate that the center of the pore is lined by predominantly hydrophobic atomic components expanding toward the IS where occlusion of the pore takes place by the ring of Y405 (DI), F960 (DII) F1449 (DIII) and F1752 (DIV) residues which are known to form the NaV1.7's activation gate (AG) (Figure 3). Macroscopically, the wide CC translates into a structural contraction event as the outer surface radius is locally minimized so that the channel is split into two funnel-like structural compartments (see trace of $L(\mathbf{p})$ on Figure 3). Hydropathic density variations can be summarized in terms of three visually-distinguishable contour domains; the $T_2^{(0)}$ domain accounting for HP's formation, the $T_1^{(0)}$ domain accounting for a hydrophobic pore wall placed between the hydrophilic selectivity filter (SF) and the hydrophilic extracellular side (ES), and the hydrophilic $T_3^{(0)}$ domain covering the largest contour map area and incorporating both the SF and the ES mouth.

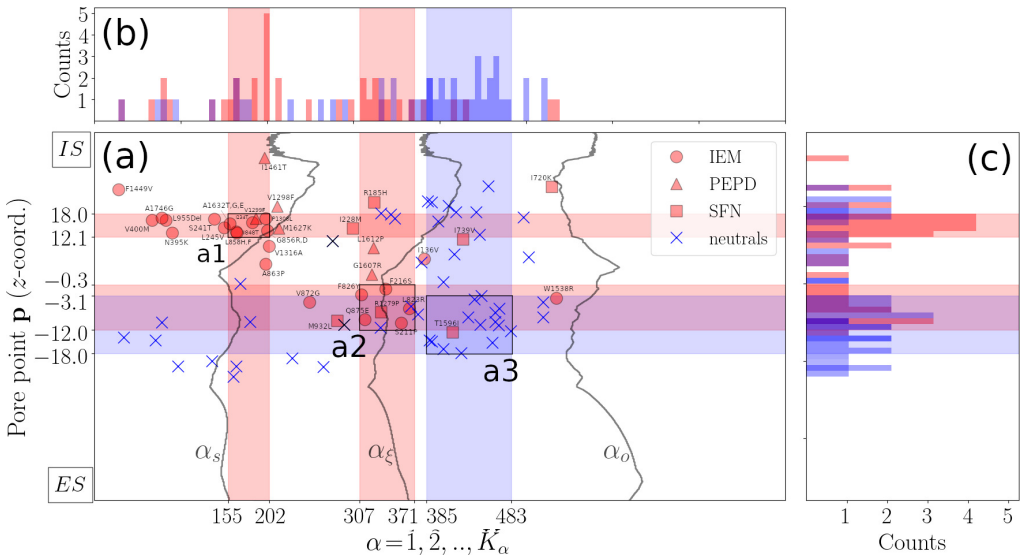

Figure 2: ***Geometrical mapping of missense SCN9A-gene mutation sites.*** *(a), Two sets of missense SCN9A-gene mutation are employed; a pain-related set containing IEM, PPD and SFN mutation sites and a neutral set containing mutation sites*

not related to pain disease (SM, S3). Lines α_s, α_ξ and α_o highlight the boundaries among consecutive domains. Map areas "a1", "a2" and "a3" indicate maximizations in density of mutation sites. (b), Histogram of mutation sites along α-direction. (c), Histogram of mutation sites along $\mathbf{p}$*-direction. Red- and blue-colored histograms account for distribution of pain-related and neutral mutation sites, respectively.*

The SF's microenvironment is formed by the residues D361 (DI), E930 (DII), K1406 (DIII) and A1698 (DIV) where a bare sodium ion of radius ≈ 1.8 Å can exactly fit in (Figure 3). Strikingly, approximately 53% of pain-related mutation sites are found within $T_2^{(0)}$ while map areas I and II are distributed along HP's boundary, i.e., occupy contour map area that belongs to both domains $T_2^{(0)}$ and $T_3^{(0)}$ (Figure 3). On the other hand, only 10% of neutral mutations sites are located within the $T_2^{(0)}$ while area III is distributed solely within $T_3^{(0)}$ (Figure 3).

Given that mutations affecting a protein's hydrophobic interior pose a high risk for detrimental destabilizations [82, 83], we hypothesize that mutations occurring at structural locations in proximity to HP are more likely to be related with pain phenotype as their perturbing effect can directly affect tight hydrophobic packing around channel's mass center. We test this hypothesis by calculating the distance between each mutation structural location and HP's boundary (SM, S8) and fed retrieved distances into a binary classifier. We achieved to classify correctly 29 (out of 36) and 38 (out of 48) of pain-related and neutral, respectively, mutations correctly with a cut-off distance of 18.13 Å (Figure 4). This translates to an area under receiver operating characteristics (ROC) curve of 0.787 and pain phenotype prediction with specificity of 0.791 and sensitivity of 0.805 (Figure 4(a)).

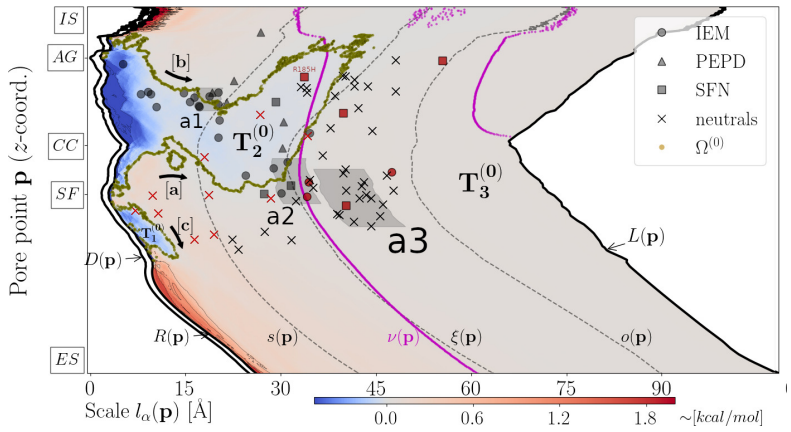

Figure 3: ***Spatial profile of the hydropathic density around NaV1.7's pore.*** *Contour map of the hydropathic density pore function, $m^{(0)}(\mathbf{p}, l_\alpha(\mathbf{p}))$, for $\mathbf{p} \in P$ and $\alpha = 1, 2, .., K_\alpha = 800$. Blue and red color contour domains represent hydrophobic and hydrophilic domains around the pore, respectively. Black lines $R(\mathbf{p})$, $\bar{R}(\mathbf{p})$ and $L(\mathbf{p})$*

depict geometrical pore characteristics. Magenta dashed line $\nu(\mathbf{p})$ represents the PMs-VSs spatial transition. Dashed black lines $s(\mathbf{p})$, $\xi(\mathbf{p})$ and $o(\mathbf{p})$ account for the boundaries between different domains (see Methods). Zero-crossing points of $m^{(0)}(\mathbf{p}, l_\alpha(\mathbf{p}))$ collected in $\Omega^{(0)}$ describe the boundaries among hydropathic domains $T_1^{(0)}$, $T_2^{(0)}$ and $T_3^{(0)}$. Pain-related and neutral mutation sites are represented by different symbols (see Legend). Mutations sites highlighted with red color correspond to misclassified events. Grey-shaded areas "a1", "a2" and "a3" highlight map ares where map density of mutation sites maximizes.

Misclassified pain-related mutations S211P, L823R, W1538R, I720K, I739V and T1596I are found outside of $T_2^{(0)}$ thus not in proximity to HP (Figure 3 and 4(b)). Only a single pain-related misclassification is found within $T_2^{(0)}$, namely, R185H (Figure 3 and 4(b)). This striking misclassification is due to the elementary statistical approach adopted for calculating distance scores which fails to capture the complex geometry of $T_2^{(0)}$ (SM, S8). Misclassified neutral mutations are V1428I, T920N, V194I, V1613I, T1398N, I1399D, S1419N, D1662A, D1674A and K1700A are found either inside $T_2^{(0)}$ or in close proximity to HP's boundary with a tendency to cluster around the SF (Figure 3 and 4(b)).

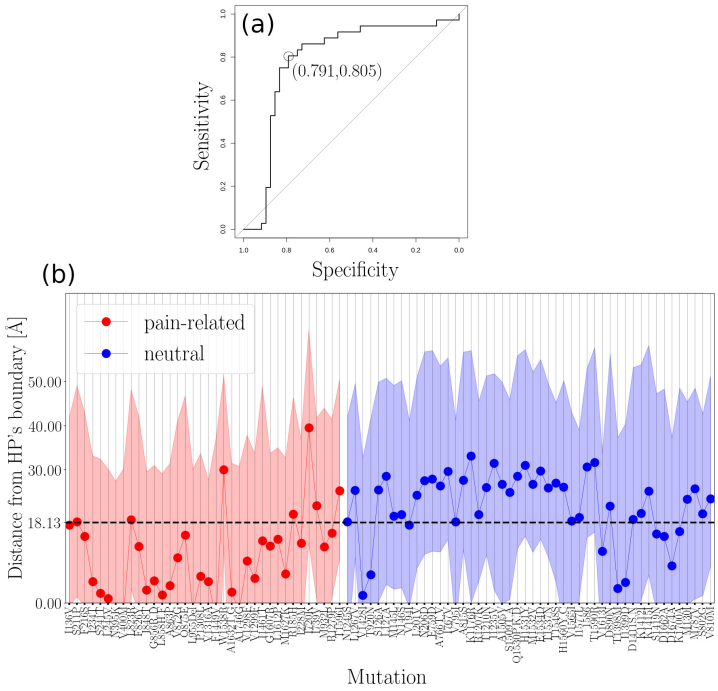

Figure 4: ***Binary classification of NaV1.7 variants based on their distance from the HP's boundary.*** *(a), ROC curve constructed based on the HP's-boundary distance data (for construction of data set see SM, S8). Optimal threshold value corresponds to specificity and sensitivity values of 0.791 and 0.805, respectively. Area under*

ROC curve is 0.787. (b), Visualization of ROC curve data. Optimal threshold value 18.13 Å is marked with black dashed line. Shaded area around distance values indicates the 95% confidence intervals. ROC curve is constructed in R [67] by using the pROC package [84].

HIs underlying atom packing around NaV1.7's pore can be adequately described in terms of the HIIS axial field component illustrated in Figure 5(a). HIIS axial field topology is organized into five domains, namely, of $T_1^{(1)}$, $T_2^{(1)}$, $T_3^{(1)}$, $T_4^{(1)}$ and $T_5^{(1)}$ (Figure 5(a)). The centrally-located $T_5^{(1)}$ domain covers the largest map area and roughly dichotomizes the contour map into two pseudo-symmetric parts, namely, an ES part incorporating $T_1^{(1)}$ and $T_3^{(1)}$ an IS part incorporating $T_2^{(1)}$ and $T_4^{(1)}$. Pain-related mutation sites are solely found within the $T_4^{(1)}$ (58%) and $T_5^{(1)}$ (42%) domains. On the other hand, neutral sites are found within the $T_3^{(1)}$ (14%), $T_4^{(1)}$ (19%) and $T_5^{(1)}$ (67%) domains.

In order to decode mutation sites clustering behavior on the contour map of Figure 5(a) we adopted a phenomenological perspective based on the existence of a critical point, $\xi(\mathbf{p}_{crit.})$, associated with the SF (SM, S9). A crucial result that motivated us to adopt such an approach is that pain-related mutation sites are attracted toward the critical point in sheer contrast to neutral mutation sites which are repelled from it (Figure 5(b)). We term this phenomenon critical clustering. Geometrically, the formation of the critical mutation sites cluster reflects the tendency of structural locations of pain-related mutations to minimize their distance from the surface of the critical sphere of radius $\xi(\mathbf{p}_{crit.}) \approx 33.4$ Å; intuitive graphical representation of this phenomenon is provided in Figure 5(a) where we show that "hot" areas I and II intersect with the dashed green line $\xi(\mathbf{p}_{crit.})$ representing critical sphere's surface (Figure 5(a)).

Armed with the observation that pain-related mutation sites (in contrast to neutrals) tend to occupy locations at critical hydropathic-interactions distance from the SF, we focused on the scaling behavior of HIIS around the critical point that is adequately described in terms of the power-law scheme

$$m_z^{(1)}(\mathbf{p}_{crit.}, l_\alpha(\mathbf{p}_{crit.})) \sim \begin{cases} l_\alpha(\mathbf{p}_{crit.})^{\gamma_{partI}(\mathbf{p}_{crit.})} \text{ for } \; s(\mathbf{p}_{crit.}) < l_\alpha(\mathbf{p}_{crit.}) \leq \xi(\mathbf{p}_{crit.}) \\ l_\alpha(\mathbf{p}_{crit.})^{\gamma_{partII}(\mathbf{p}_{crit.})} \text{ for } \; \xi(\mathbf{p}_{crit.}) < l_\alpha(\mathbf{p}_{crit.}) \leq o(\mathbf{p}_{crit.}) \end{cases} \tag{r1}$$

accounting for a HIs-network expansion and contraction within the pre- and post-inflection phase intervals $s(\mathbf{p}_{crit.}) < l_\alpha(\mathbf{p}_{crit.}) \leq \xi(\mathbf{p}_{crit.})$ and $\xi(\mathbf{p}_{crit.}) < l_\alpha(\mathbf{p}_{crit.}) \leq o(\mathbf{p}_{crit.})$ with rates of $\gamma_{partI}(\mathbf{p}_{crit.}) = 2.27 \pm 0.18$ and $\gamma_{partII}(\mathbf{p}_{crit.}) = -5.18 \pm 1.02$, respectively (Figure 5(c)). On the left of the interval $\xi(\mathbf{p}_{crit.}) < l_\alpha(\mathbf{p}_{crit.}) \leq \nu(\mathbf{p}_{crit.})$, both, the range and intensity of HIIS maximize as the HIs-network configuration exceeds its critical size marking the transition from the pre-inflection phase toward the post-inflection phase. The energy levels

associated with this phase transition are given by

$$U(\mathbf{p}_{crit.}, l_\alpha(\mathbf{p}_{crit.})) \sim \begin{cases} N(\mathbf{p}_{crit.}, l_\alpha(\mathbf{p}_{crit.})) \cdot l_\alpha(\mathbf{p}_{crit.})^{\gamma_{partI}(\mathbf{p}_{crit.})-1} \text{ for } s(\mathbf{p}_{crit.}) < l_\alpha(\mathbf{p}_{crit.}) \leq \xi(\mathbf{p}_{crit.}) \\ N(\mathbf{p}_{crit.}, l_\alpha(\mathbf{p}_{crit.}) \cdot l_\alpha(\mathbf{p}_{crit.})^{\gamma_{partII}(\mathbf{p}_{crit.})-1} \text{ for } \xi(\mathbf{p}_{crit.}) < l_\alpha(\mathbf{p}_{crit.}) \leq o(\mathbf{p}_{crit.}) \end{cases} \tag{r2}$$

where $N(\mathbf{p}_{crit.}, l_\alpha(\mathbf{p}_{crit.})$ can be replaced with its best-fitted Richards model, $n_{ric}(\mathbf{p}_{crit.}, l_\alpha(\mathbf{p}_{crit.}))$ (see caption of Figure 5 for Richards model parameters), providing with an estimation of the atom-packing energy (AE) (Figure 5(c)). Similarly to the NaVAb case [66], AE maximization occurs in the vicinity of the interval $\xi(\mathbf{p}_{crit.}) < l_\alpha(\mathbf{p}_{crit.}) \leq \nu(\mathbf{p}_{crit.})$ so that energetic coupling of the PMs with the VSs is dictated by the phase transition (Figure 5(c),(d)).

Equation r1 indicates that inter-atomic HIs law is robust to microscopic modifications of the atomic structure, e.g., addition, removal or deletion of a small number of atoms corresponding to small-amplitude perturbations of $N(\mathbf{p}_{crit.}, l_\alpha(\mathbf{p}_{crit.}))$ [85]. This happens however at the cost of re-tuning HI-cIS and, hence, also of AE that, in the case of small-amplitude perturbations of $N(\mathbf{p}_{crit.}, l_\alpha(\mathbf{p}_{crit.}))$, are expected to be up- and down-regulated toward and away from the critical point, respectively, in a power-law fashion described by r2 (Figure 5(c)). Mutation-induced perturbations propagating throughout the structure are thus expected to be amplified in the vicinity of the critical point while, on the other hand, to be damped out toward the interior (i.e., toward the HP and the SF) and toward channel exterior bounded by outer pore surface radius. Given that mutations in the structural proximity of the SF are highly likely to have a deleterious LOF effect [86], observed damping-out mechanism might act as a shield protecting SF's biological machinery from mutations occurring within the pre-inflection phase. On the other hand, mutations occurring in the post-inflection phase are unlikely to affect the SF as they have to overcome a large energy barrier in order to reach channel interior. We thus hypothesize that critical clustering of pain-related mutations might actually reflect a trade-off between the two extremes; a destructive destabilization and an insignificant one.

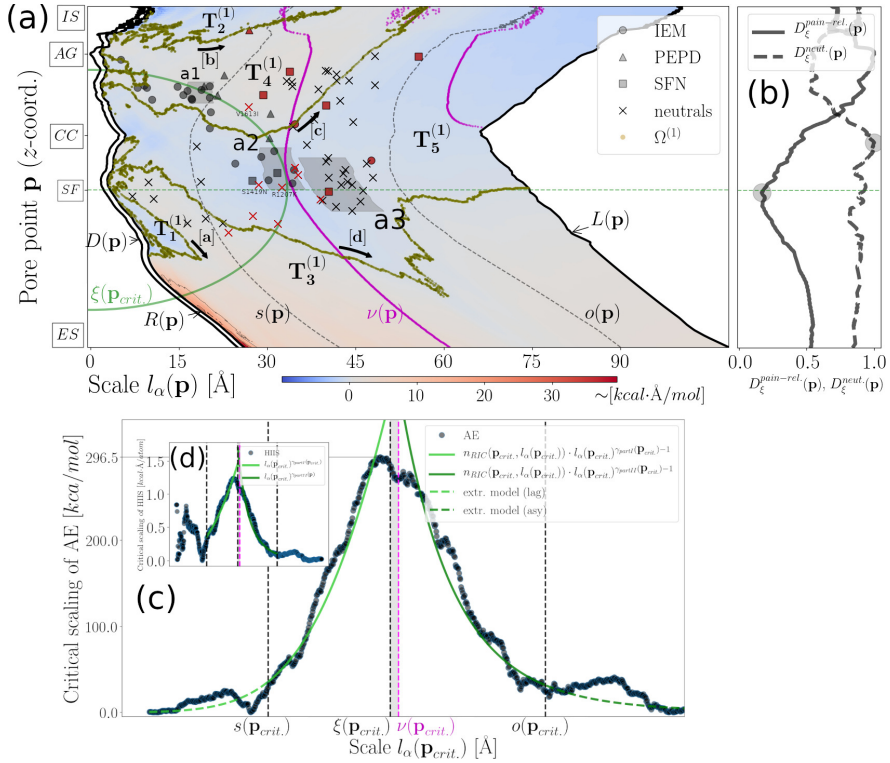

Figure 5: ***Spatial profile of HIIS along NaV1.7's pore.*** *(a), Contour map of HIIS axial part,* $m_z^{(1)}(\mathbf{p}, l_\alpha(\mathbf{p}))$*, for* $\mathbf{p} \in P$ *and* $\alpha = 1, 2, .., K_\alpha = 800$*. Blue and red color contour domains represent represent configurations of* $\vec{\boldsymbol{m}}_z^{(1)}(\mathbf{p}, l_\alpha(\mathbf{p}))$ *with orientation "out" and "in", respectively. Black lines* $R(\mathbf{p})$*,* $\bar{R}(\mathbf{p})$ *and* $L(\mathbf{p})$ *depict geometrical pore characteristics. Magenta dashed line* $\nu(\mathbf{p})$ *represents the PMs-VSs spatial transition. Dashed black lines* $s(\mathbf{p})$*,* $\xi(\mathbf{p})$ *and* $o(\mathbf{p})$ *account for the boundaries between different domains.* $\xi(\mathbf{p}_{crit.})$ *represents the critical radius. Black arrows* [a]*,* [b]*,* [c]*,* [d] *and* [e] *indicate the clustering behavior of the zero-crossing points of* $m_z^{(1)}(\mathbf{p}, l_\alpha(\mathbf{p}))$ *collected in* $\Omega^{(1)}$ *describing boundaries among contour domains* $T_1^{(1)}$*,* $T_2^{(1)}$*,* $T_3^{(1)}$*,* $T_4^{(1)}$ *and* $T_5^{(1)}$*. Mutations sites highlighted with red color correspond to misclassified events. Grey-shaded areas "a1", "a2" and "a3" highlight map ares where map density of mutation sites maximizes. (b), Distance between inflection points and mutation sites along the pore is also plotted in terms of the normalized (with respect to maximum value) statistical representations* $\bar{D}_\xi^{path.}(\mathbf{p})$ *and* $\bar{D}_\xi^{cont.}(\mathbf{p})$*, respectively. (c), Power-law scaling of HIIS axial part for* $\mathbf{p}_{crit.} = (\mathrm{p}_x \approx 0, \mathrm{p}_y \approx 0, \mathrm{p}_z = -12.1)$*. The best-fitting first-part-inflection-domain and second-part-inflection-domain power-law approximations are also plotted with mean absolute relative fitting errors being* 0.09 ± 0.01 *and* 0.15 ± 0.03*, respectively. (d), Power-law-like behavior of AE,* $U(\mathbf{p}, l_\alpha(\mathbf{p}))$ *for* $\mathbf{p}_{crit.} = (\mathrm{p}_x \approx 0, \mathrm{p}_y \approx 0, \mathrm{p}_z = -12.1)$*. First- and second-part-inflection-domain modeling approximations of AE are also plotted with their mean absolute relative modeling errors being* 0.11 ± 0.02 *and* 0.14 ± 0.03*, respectively. AE model extrapolation toward the*

lag-domain $l_\alpha(\mathbf{p}) \leq s(\mathbf{p})$ *and the asymptote-domain* $l_\alpha(\mathbf{p}) > o(\mathbf{p})$ *result in a mean absolute relative fitting error of* 6.06 ± 16.0 *and* 1.55 ± 6.39*, respectively. Richards model parameters used for modeling AE are* $\{A(\mathbf{p}_{crit.}) = 1.03, t(\mathbf{p}_{crit.}) = 0.03, s(\mathbf{p}_{crit.}) = 18.16, \tilde{q}(\mathbf{p}_{crit.}) = 0.47\}$.

We tested the critical-clustering hypothesis by calculating the distance each mutation structural location and SF's critical point (SM, S8), and feeding retrieved distances into a binary classifier. We achieved to classify correctly 28 (out of 36) and 39 (out of 48) of pain-related and neutral mutations correctly with a cut-off distance of 5.8 Å . This translates to an area under receiver operating characteristics (ROC) curve of 0.824 and pain phenotype prediction with specificity of 0.812 and sensitivity of 0.777 (Figure 6(a)). Intuitive geometrical depiction of this result requires to think of a "hot" spherical shell squeezed between the spheres of radii $\xi(\mathbf{p}_{crit.})+5.8$ Å and $\xi(\mathbf{p}_{crit.})-5.8$ Å centered at $\mathbf{p}_{crit.}$ incorporating areas I and II thus containing the majority of pain-related structural locations. This tendency can be deduced from Figure 5 where we can see that correctly-classified pain-related and neutral sites tend to minimize and maximize, respectively, their distance from the critical radius $\xi(\mathbf{p}_{crit.})$. The opposite holds for misclassified mutations. Note however that due to the pore points offset, distances of sites from $\xi(\mathbf{p}_{crit.})$ line on Figure 5 are not equal with the distances of their structural locations from the surface of the sphere of $\xi(\mathbf{p})$ (discrepancies are of order $\approx 3.13 \pm 4.63$ Å). Misclassified pain-related mutations are I136V, W1538R, I1461T, R185H, I228M, I720K, I739V and T1596I indicating that sensitivity output is qualitatively similar to the HP-based classification attempt. On the other hand, quality of specificity differs significantly among classification attempts as critical-point distance criterion misclassified neutrals M145L, M146S, R1207K, T1210N, V1613I, D890N, K1412I, K1415I and S1419N are clustering within the "hot" spherical shell in proximity to HP's boundary.

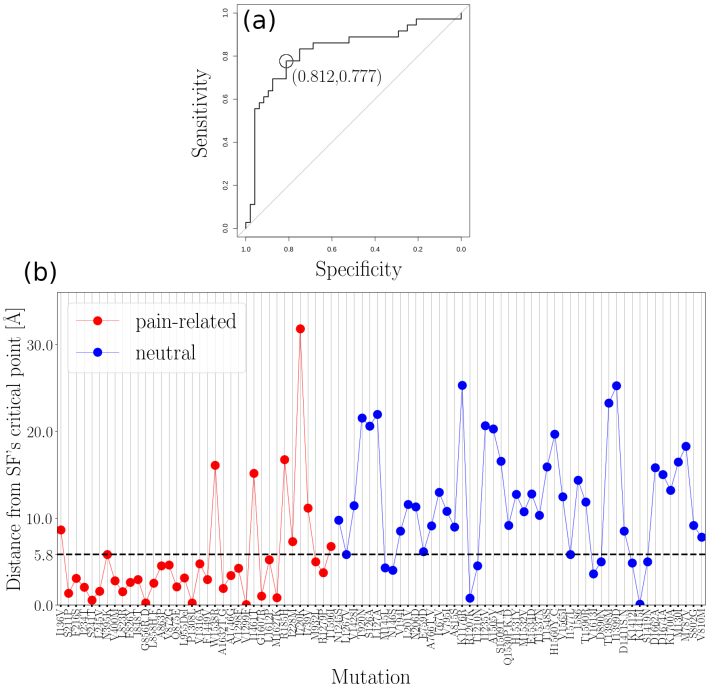

Figure 6: ***Binary classification of NaV1.7 variants based on their distance from SF's critical point.*** *(a), ROC curve constructed based on SF's-critical-point distance data (for construction of data set see SM, S8). Optimal threshold value 5.8 Å corresponds to specificity and sensitivity values of 0.812 and 0.777, respectively. Area under ROC curve is 0.824. (b), Visualization of ROC curve data. Optimal threshold value 5.8 Å is marked with black dashed line. ROC curve is constructed in R [67] by using the pROC package [84].*

Finally, in order to harvest the classification power of both predictors, we linearly combined distance metrics by calculating a weighted distance average (SM, S10). The weighted distance average achieved to classify correctly 29 (out of 36) pain-related mutations and 45 (out of 48) neutrals, i.e., sensitivity = 0.805, specificity = 0.937, area under ROC curve = 0.872 (Figure 7(a)). The threshold weighted distance value is 9.6 Å and it indicates which mutations are found in proximity to SF's critical point and HP's boundary.

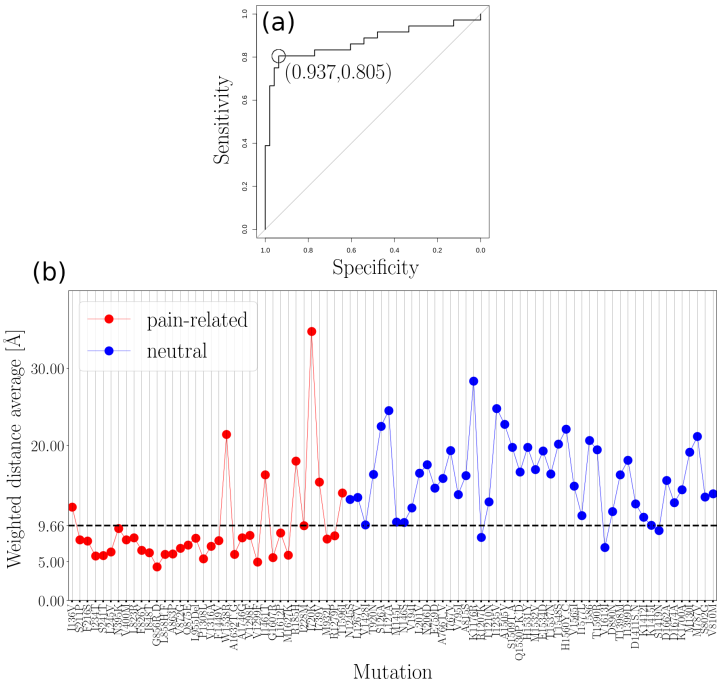

Figure 7: ***Binary classification of NaV1.7 variants based on the weighted distance average.*** *(a), ROC curve constructed based on weighted distance data (for construction of data set see SM, S8). Optimal threshold value 9.6 Å corresponds to specificity and sensitivity values of 0.805 and 0.937, respectively. Area under ROC curve is 0.872. (b), Visualization of ROC curve data. Optimal threshold value 9.6 Å is marked with black dashed line. ROC curve is constructed in R [67] by using the pROC package [84].*

The relatively-low sensitivity of the weighted distance average is not surprising if we consider that both classifications attempts failed in correctly classifying pain-related mutations found far away from the HP and from the SF; misclassified pain-related mutations are I136V, W1538R, I1461T, R185H, I720K, I739V and T1596I and all of them are found within the post-inflection phase with the exception of I1461T which is located within the lag domain but still far away from the HP and from the SF (Figure 3, 5(a) and 7). On the other hand, misclassified neutrals R1207K, V1613I and S1419N occupy "hot" spots located in proximity to SF's critical point and HP's boundary (Figure 3, 5(a) and 7).

Discussion and concluding remarks

Criticality hypothesis in biology aims at explaining how emergence of power-laws increases biological system's robustness and efficiency hand-in-hand with evolution. Empirical evidence for complex biological systems operating near critical points include cases of gene expression [87], DNA sequences [88], protein

structures [60, 61, 62, 63], cell growth [89] and neuronal dynamics underlying brain activity [90]. In practice, criticality implies that system dynamics are delicately balanced between an ordered state where perturbations are damped-out and a disordered state where perturbations are amplified. Consequences of critical dynamics are associated with optimal information processing [91], enhanced network stability [92] and maximal sensitivity to external stimuli [93].

In this work, instead of trying to predict the effect of missense *SCN9A*-gene mutations via comparing mutant NaV1.7 structures *in silico*, we extracted hydropathic features of the wild-type atomic environment encoding NaV1.7's response to mutation-induced variations. Stated differently, we hypothesized that some regions of the atomic environment around NaV1.7's pore exhibit higher sensitivity to mutation-induced perturbations due to the long-range nature of HIs guaranteeing their stability; a hallmark of SOC is that avalanche-like perturbing effects are amplified and fast-spreading throughout critical network locations [94]. To test this hypothesis we mapped mutation structural locations on their corresponding mutation sites and probed topological and scaling hydropathic characteristics of the atomic bulk around the pore. Importantly, this is possible due to the relatively-large number of pain-related mutations providing with the opportunity of structure-based mutation statistics and, consequently, identification of densely-populated (by mutation sites) structural domains.

The starting point of the presented procedures was the approximation of the atomic cumulative distribution function around NaV1.7's pore demonstrating that packing of atoms follows a sigmoid accumulation pattern. The generality of the Richards model was found to be adequate for this modeling purpose verifying the sigmoid accumulation hypothesis and, consequently, revealing a biphasic spatial organization of the atomic environment around the pore dictated by the spatial transition from the PM from the VSs. We showed that the pore is lined by a HP dominating within channel interior and that HIs stabilizing atom-packing around the SF are critically tuned with respect to the local inflection points. This NaV1.7 feature is shared with its evolutionary-ancestor, namely, with the pre-open NaVAb channel, suggesting that HIs scale-invariance might be conserved from NaVChs of bacterial homomers to NaVChs of mammalian heteromers [66].

Pain-related mutations tend to occupy structural locations in proximity to the HP while maintaining a critical HIs-distance from the SF. Geometrically, this result indicates that the majority of pain-related mutations are found within a spherical shell around the SF incorporating parts of the HP. What might be the evolutionary principle underlying this non-random mutation distribution around NaV1.7's pore? Given that the DEKA SF sequence is conserved among human and non-human NaVCh templates [95], we propose that expression of mutations at critical hydropathic-interactions distance from the SF might reflect an evolutionary trade-off between potentially-deleterious destabilizations occurring too close to the SF and insignificant polymorphisms occurring far away from it. According to this rationale, mutations occupying critical hydropathic-interactions network locations lead to a GOF effect by increasing channel's configuration space and, consequently, expanding physiological range of ionic currents, while

not risking structure deletion or severe destabilizations that can induce a LOF effect [86].

Misclassification of seven pain-related events found within the post-inflection phase (namely, of I136V, W1538R, I1461T, R185H, I720K, I739V and T1596I) suggests that the destabilizing mutation effect within the post-inflection phase and, specifically, within the VSs needs to be locally investigated. In particular, misclassified pain-related events are likely to affect local properties of the VSs which are however crucial for physiological gating and ionic currents. It might therefore be useful for future studies to consider a decoupling of the PM from the VSs in order to focus solely on the cumulative hydropathic topology and HIs-networking within the VSs. Moreover, a goal for follow-up studies is to include biophysical characteristics of substituted amino acids (e.g., size, charge, hydropathicity-property, degree of conservation) into our model as this might not only improve classification accuracy but also provide with a more detailed picture of the mutation effect.

Admittedly, a limitation of this study is the small (from a statistics point of view) number of available mutation events. To resolve this issue and provide with stronger statistical validation, we may consider in future studies to increase number of neutral and pain-related mutations, for example, by introducing NaV1.7 variants found in the Genome Aggregation Database (gnomAD) [96]. A methodological weakness is that we neglected radial hydropathic effects. In particular, even if the amplitude of the radial HIIS component is small in comparison to the amplitude of the axial HIIS component, its role might be non-negligible for interactions between ions and pore walls. Moreover, it is important to remind at this point that we chose to work with a closed-state structural model of the NaV1.7 which most likely corresponds to a pre-open state of NaV1.7's gating cycle. The rationale underlying this choice was that we sought to establish a connection (if any) between the closed-state NaV1.7 and the closed-state NaVAb before we focus on the human NaV1.7 structure captured at an inactivated state [95].

Our findings suggest that pathogenicity of NaV1.7 variants can be predicted if corresponding mutation structural locations are in structural and, hence, also hydropathic proximity to either the HP or the SF. Prediction of pathogenicity can then be performed with negligible computational effort and similar or even higher accuracy to [56] (reported accuracy: 0.81) but also to the more recent study of [97] where a MLE computational pipeline was employed (reported accuracy on the human NaV1.7 template: 63.5%). In an era where MLE pipelines become increasingly popular, the phenomenological framework curated in this study could provide biophysical rationalization to MLE-retrieved predictions for NaVCh pathophysiological characterization; crucially, hydropathicity-property is recognized as a key-feature for predicting functional effects of genetic defects in NaVChs, as well as, in voltage-gated calcium channels [86].

Declarations

Ethics approval and consent to participate

Not applicable.

Consent for publication

Not applicable.

Availability of data and materials

Data sharing is not applicable to this article as no datasets were generated or analyzed during the current study. The 3D structural model of the NaV1.7 channel is available from the authors with permission of YY and SGW.

Competing interests

The authors declare that they have no competing interests.

Funding

The study was partly funded by the European Union 7th Framework Programme (grant n602273).

Authors' contributions

MNX designed the study, performed computations and data analysis. RW and PL contributed to refinement of algorithmic steps. YY provided with the 3D structural model of the NaV1.7 channel, MMG contributed to variants selection and analysis, RW, PL, DK, YY, JH, HJS and SGW provided with critical feedback and helped with the interpretation of the results; YY and SGW encouraged MNX to focus on specific aspects of the findings. HJS supervised the study. GL and CGF were in charge of overall direction. MNX wrote the manuscript in consultation with all the co-authors. All co-authors have critically revised the manuscript.

Acknowledgments

We acknowledge technical and scientific support provided by the PROPANE study group.

References

[1] Cheng, X., Dib-Hajj, S.D., Tyrrell, L., Waxman, S.G. Mutation I136V alters electrophysiological properties of the Na(v)1.7 channel in a family with onset of erythromelalgia in the second decade. *Mol Pain* **4**, 1 (2008).

[2] Estacion, M., Choi, J.S., Eastman, E.M. et al. Can robots patch-clamp as well as humans? Characterization of a novel sodium channel mutation. *J Physiol* **588**, 1915-1927 (2010).

[3] Wu, M.T., Huang, P.Y., Yen, C.T., Chen, C.C., Lee, M.J. A novel SCN9A mutation responsible for primary erythromelalgia and is resistant to the treatment of sodium channel blockers. *PLoS One* **8**, e55212 (2013).

[4] Choi, J.S., Dib-Hajj, S.D., Waxman, S.G. Inherited erythermalgia: limb pain from an S4 charge-neutral Na channelopathy. *Neurology* **67**, 1563-1567 (2006).

[5] Ahn, H.S., Dib-Hajj, S.D., Cox, J.J. et al. A new Nav1.7 sodium channel mutation I234T in a child with severe pain. *Eur J Pain* **14**, 944-950 (2010).

[6] Lampert, A., Dib-Hajj, S.D., Tyrrell, L., Waxman, S.G. Size matters: Erythromelalgia mutation S241T in Nav1.7 alters channel gating. *J Biol Chem* **281**, 36029-36035 (2006).

[7] Yang,,Y., Dib-Hajj, S.D., Zhang, J. et al. Structural modelling and mutant cycle analysis predict pharmacoresponsiveness of a Na(V)1.7 mutant channel. *Nat Commun* **3**, 1186 (2012).

[8] Emery, E.C., Habib, A.M., Cox, J.J. et al. Novel SCN9A mutations underlying extreme pain phenotypes: unexpected electrophysiological and clinical phenotype correlations. *J Neurosci* **35**, 7674-7681 (2015).

[9] Sheets, P.L., Jackson, J.O. 2nd, Waxman, S.G., Dib-Hajj, S.D., Cummins, T.R. A Nav1.7 channel mutation associated with hereditary erythromelalgia contributes to neuronal hyperexcitability and displays reduced lidocaine sensitivity. *J Physiol* **581**, 1019-1031 (2007).

[10] Fischer, T.Z., Gilmore, E.S., Estacion, M. et al. A novel Nav1.7 mutation producing carbamazepine-responsive erythromelalgia. *Ann Neurol* **65**, 733-741 (2009).

[11] Lampert, A., Dib-Hajj, S.D., Eastman, E.M., Tyrrell, L., Lin, Z., Yang, Y., Waxman, S.G. Erythromelalgia mutation L823R shifts activation and inactivation of threshold sodium channel Nav1.7 to hyperpolarized potentials. *Biochem Biophys Res Commun* **390**, 319-324 (2006)..

[12] Wu, B., Zhang, Y., Tang, H. et al. A Novel SCN9A Mutation (F826Y) in Primary Erythromelalgia Alters the Excitability of Nav1.7. *Curr Mol Med* **17**, 450-457 (2017).

[13] Cummins, T.R., Dib-Hajj, S.D., Waxman, S.G. Electrophysiological properties of mutant Nav1.7 sodium channels in a painful inherited neuropathy. *J Neurosci* **24**, 8232-8236 (2004).

[14] Han, C., Dib-Hajj, S.D., Lin, Z. et al. Early- and late-onset inherited erythromelalgia: genotype-phenotype correlation. *Brain* **132**, 1711-1722 (2009).

[15] Theile, J.W., Cummins, T.R. Inhibition of Navβ4 peptide-mediated resurgent sodium currents in Nav1.7 channels by carbamazepine, riluzole, and anandamide. *Mol Pharmacol* **80**, 724-734 (2011).

[16] Tanaka, B.S., Nguyen, P.T., Zhou, E.Y. et al. Gain-of-function mutation of a voltage-gated sodium channel NaV1.7 associated with peripheral pain and impaired limb development. *J Biol Chem* **292**, 9262-9272 (2017).

[17] Hoeijmakers, J.G., Han, C., Merkies, I.S. et al. Small nerve fibres, small hands and small feet: a new syndrome of pain, dysautonomia and acromesomelia in a kindred with a novel NaV1.7 mutation. *Brain* **135**, 345-358 (2012).

[18] Cummins, T.R., Dib-Hajj, S.D., Waxman, S.G. Electrophysiological properties of mutant Nav1.7 sodium channels in a painful inherited neuropathy. *J. Neurosci* **24**, 8232-8236 (2004).

[19] Rush, A.M., Dib-Hajj, S.D., Liu, S., Cummins, T.R., Black, J.A., Waxman, S.G. A single sodium channel mutation produces hyper- or hypoexcitability in different types of neurons. *Proc Nat Acad Sci USA* **103**, 8245-8250 (2006).

[20] Han, C., Rush, A.M., Dib-Hajj, S.D. et al. Sporadic onset of erythermalgia: a gain-of-function mutation in Nav1.7. *Ann Neurol* **59**, 553-558 (2006).

[21] Harty, T.P., Dib-Hajj, S.D., Tyrrell, L., Blackman, R., Hisama, F.M., Rose, J.B., Waxman, S.G. $Na_V1.7$ mutant A863P in erythromelalgia: effects of altered activation and steady-state inactivation on excitability of nociceptive dorsal root ganglion neurons. *J Neurosci* **26**, 12566-12575 (2006).

[22] Choi, J.S., Zhang, L., Dib-Hajj, S.D. et al. Mexiletine-responsive erythromelalgia due to a new Na(v)1.7 mutation showing use-dependent current fall-off. *Exp Neurol* **216**, 383-389 (2009).

[23] Stadler, T., O'Reilly, A.O., Lampert, A. Erythromelalgia mutation Q875E Stabilizes the activated state of sodium channel Nav1.7. *J Biol Chem* **290**, 6316-6325 (2015).

[24] Cheng, X., Dib-Hajj, S.D., Tyrrell, L., Te Morsche, R.H., Drenth, J.P., Waxman, S.G. Deletion mutation of sodium channel Na(V)1.7 in inherited erythromelalgia: enhanced slow inactivation modulates dorsal root ganglion neuron hyperexcitability. *Brain* **134**, 1972-1986 (2011).

[25] Cheng, X., Dib-Hajj, S.D., Tyrrell, L., Wright, D.A., Fischer, T.Z., Waxman, S.G. Mutations at opposite ends of the DIII/S4-S5 linker of sodium channel NaV1.7 produce distinct pain disorders. *Mol Pain* **6**, 24 (2010).

[26] Estacion, M., Yang, Y., Dib-Hajj, S.D. et al. A new Nav1.7 mutation in an erythromelalgia patient. *Biochem Biophys Res Commun* **432**, 99-104 (2013).

[27] Wu, M.T., Huang, P.Y., Yen, C.T., Chen, C.C., Lee, M.J. A novel SCN9A mutation responsible for primary erythromelalgia and is resistant to the treatment of sodium channel blockers. *PLoS One* **8**, e55212 (2013).

[28] Dib-Hajj, S.D., Rush, A.M., Cummins, T.R. et al. Gain-of-function mutation in Nav1.7 in familial erythromelalgia induces bursting of sensory neurons. *Brain* **128**, 1847-1854 (2005).

[29] Cregg, R., Laguda, B., Werdehausen, R. et al. Novel mutations mapping to the fourth sodium channel domain of Nav1.7 result in variable clinical manifestations of primary erythromelalgia. *Neuromolecular Med* **15**, 265-278 (2013).

[30] Eberhardt, M., Nakajima, J., Klinger, A.B. et al. Inherited pain: sodium channel Nav1.7 A1632T mutation causes erythromelalgia due to a shift of fast inactivation. *J Biol Chem* **289**, 1971-1980 (2014).

[31] Yang, Y., Huang, J., Mis, M.A. et al. Nav1.7-A1632G Mutation from a Family with Inherited Erythromelalgia: Enhanced Firing of Dorsal Root Ganglia Neurons Evoked by Thermal Stimuli. *J Neurosci* **36**, 7511-7522 (2016).

[32] Jarecki, B.W., Sheets, P.L., Jackson, J.O. 2nd, Cummins, T.R. Paroxysmal extreme pain disorder mutations within the D3/S4-S5 linker of Nav1.7 cause moderate destabilization of fast inactivation. *J Physiol* **586**, 4137-4153 (2008).

[33] Jarecki, B.W., Sheets, P.L., Jackson, J.O. 2nd, Cummins, T.R. Paroxysmal extreme pain disorder mutations within the D3/S4-S5 linker of Nav1.7 cause moderate destabilization of fast inactivation. *J Physiol* **586**, 4137-4153 (2008).

[34] Theile, J.W, Jarecki, B.W., Piekarz, A.D., Cummins, T.R. Nav1.7 mutations associated with paroxysmal extreme pain disorder, but not erythromelalgia, enhance Navβ4 peptide-mediated resurgent sodium currents. *J Physiol* **589**, 597-608 (2011).

[35] Fertleman, C.R., Baker, M.D., Parker, K.A. et al. SCN9A mutations in paroxysmal extreme pain disorder: allelic variants underlie distinct channel defects and phenotypes. *Neuron* **52**, 767-774 (2006).

[36] Choi, J.S., Boralevi, F., Brissaud, O. et al. Paroxysmal extreme pain disorder: a molecular lesion of peripheral neurons. *Nat Rev Neurol* **7**, 51-55 (2011).

[37] Suter, M.R., Bhuiyan, Z.A., Laedermann, C.J. et al. p.L1612P, a novel voltage-gated sodium channel Nav1.7 mutation inducing a cold sensitive paroxysmal extreme pain disorder. *Anesthesiology* **122**, 414-423 (2015).

[38] Dib-Hajj, S.D., Estacion, M., Jarecki, B.W. et al. Paroxysmal extreme pain disorder M1627K mutation in human Nav1.7 renders DRG neurons hyperexcitable. *Mol Pain* **4**, 37 (2008).

[39] Estacion, M., Dib-Hajj, S.D., Benke, P.J. et al. NaV1.7 gain-of-function mutations as a continuum: A1632E displays physiological changes associated with erythromelalgia and paroxysmal extreme pain disorder mutations and produces symptoms of both disorders. *J Neurosci* **28**, 1079-11088 (2008).

[40] Han, C., Hoeijmakers, J.G., Liu, S. et al. Functional profiles of SCN9A variants in dorsal root ganglion neurons and superior cervical ganglion neurons correlate with autonomic symptoms in small fibre neuropathy. *Brain* **135**, 2613-2628 (2012).

[41] Estacion, M., Han, C., Choi, J.S. et al. Intra- and interfamily phenotypic diversity in pain syndromes associated with a gain-of-function variant of NaV1.7. *Mol Pain* **7**, 92 (2011).

[42] Faber, C.G., Hoeijmakers, J.G., Ahn, H.S. et al. Gain of function Nav1.7 mutations in idiopathic small fiber neuropathy. *Ann. Neurol.* **71**, 26-39 (2012).

[43] Huang, J., Yang, Y., Dib-Hajj, S.D. et al. Depolarized inactivation overcomes impaired activation to produce DRG neuron hyperexcitability in a Nav1.7 mutation in a patient with distal limb pain. *J Neurosci* **34**, 12328-12340 (2014).

[44] Blesneac, I., Themistocleous, A.C., Fratter, C. et al. Rare NaV1.7 variants associated with painful diabetic peripheral neuropathy. *Pain* **159**, 469-480 (2018).

[45] Cox J.J., Reimann, F., Nicholas, A.K. et al. An SCN9A channelopathy causes congenital inability to experience pain. *Nature* **444**, 894-898 (2006).

[46] Goldberg, Y.P., MacFarlane, J., MacDonald, M.L. et al. Loss-of-function mutations in the NaV1.7 gene underlie congenital indifference to pain in multiple human populations. *Clin Genet* **71**, 311-319 (2007).

[47] Nilsen, K.B., Nicholas, A.K., Woods, C.G., Mellgren, S.I., Nebuchennykh, M., Aasly, J. Two novel SCN9A mutations causing insensitivity to pain. *Pain* **143**, 155-158 (2009).

[48] Hammer, M.U., Anderson, T.H., Chaimovich, A., Shell, M.S., Israelachvili, J. The search for the hydrophobic force law. *Faraday Discuss* **146**, 299-308 (2010).

[49] Hummer, G., Garde, S., García, A.E., Paulaitis, M.E., Pratt, L.R. Hydrophobic Effects on a Molecular Scale. *J Phys Chem B* **102**, 51 (1998).

[50] Aryal, P., Sansom M.S.P,Tucker, S.J. Hydrophobic Gating in Ion Channels. *J Mol Biol* **427**, 121-130 (2015).

[51] Li, E., Wimley, W.C., Hristova, K. Transmembrane helix dimerization:beyond the search for sequence motifs. *Biochim Biophys Acta* **1818**, 183-193 (2012).

[52] Lin, J., Motylinski, J., Krauson, A. J., Wimley, W. C., Searson, P.C., Hristova, K. Interactions of membrane active peptides with planar supported bilayers: an impedance spectroscopy study. *Langmuir* **28**, 6088-6096 (2012).

[53] Yonkunas, M., Kurnikova, M. The hydrophobic effect contributes to the closed state of a simplified ion channel through a conserved hydrophobic patch at the pore-helix crossing. *Front Pharmacol* **6**, 284 (2015).

[54] Lampert, A., O'Reilly, A.O., Dib-Hajj, S.D., Tyrrell, L., Wallace, B.A., Waxman, S.G. A Pore-blocking Hydrophobic Motif at the Cytoplasmic Aperture of the Closed-state Nav1.7 Channel Is Disrupted by the Erythromelalgia-associated F1449V Mutation. *J Biol Chem* **283**, 24118-24127 (2008).

[55] Yang, Y., Estacion, M., Dib-Hajj, S.D., Waxman, S.G. Molecular Architecture of a Sodium Channel S6 Helix: radial tuning of the voltage-gated sodium channel 1.7 activation gate. *J Biol Chem* **288**, 13741-13747 (2013).

[56] Kapetis, D., Yang, Y., Sassone, J. et al. Network topology of NaV1.7 mutations in sodium channel-related painful disorders. *BMC Systems Biology* **11**, 28 (2017).

[57] Hasan S., Hunter T., Hunter G., Pessia M., D'Adamo M.C. Commentary: A channelopathy mutation in the voltage-sensor discloses contributions of a conserved phenylalanine to gating properties of Kv1.1 channels and ataxia. *Front Cell Neurosci* **12**, 174 (2018).

[58] Payandeh, J., Scheuer, T., Zheng, N., Catterall, W.A. The crystal structure of a voltage-gated sodium channel. *Nat* **475**, 353-358 (2011).

[59] Bak, P., Tang, C., Wiesenfeld, K. Self-organized criticality: an explanation of 1/f noise. *Phys Rev Lett* **59**, 381-384 (1987).

[60] Phillips, J.C. Scaling and self-organized criticality in proteins I. *Proc Natl Acad Sci USA* **106**, 3107-3112 (2009).

[61] Phillips, J.C. Scaling and self-organized criticality in proteins II. *Proc Natl Acad Sci USA* **106**, 3113-3118 (2009).

[62] Morett, M. Self-organized critical model for protein folding. *Physica A* **390**, 3055-3059 (2011).

[63] Phillips, J.C. Self-organized criticality in proteins: Hydropathic roughening profiles of G-protein-coupled receptors. *Phys Rev E* **87**, 032709 (2013).

[64] Zhou, R., Silverman, B.D., Royyuru, A.K., Athma, P. Spatial profiling of protein hydrophobicity: Native vs. decoy structures. *Proteins* **52**, 561-572 (2003).

[65] Xenakis, M.N., Kapetis, D., Yang, Y. et al. Cumulative hydropathic topology of a voltage-gated sodium channel at atomic resolution. *Proteins*, 1319-1328, (2020).

[66] Xenakis, M.N., Kapetis, D., Yang, Y. et al. Non-extensitivity and criticality of atomic hydropathicity around a voltage-gated sodium channel's pore; a modeling study. Under review in *J Biol Phys*.

[67] R Core Team *R: A language and environment for statistical computing*. R Foundation for Statistical Computing, Vienna, Austria. `http://www.R-project.org/` (2014).

[68] Humphrey, W., Dalke, A., Schulten K. VMD-Visual Molecular Dynamics. *J Molec Graph* **14**, 33-38 (1996).

[69] Loss, R.D. Atomic weights of the elements 2001 (IUPAC technical report). *Pure Appl Chem* **73**, 667-683 (2001).

[70] Bondi, A. Van der Waals volumes and radii. *J Phys Chem* **68**, 441-51 (1964).

[71] Rowland, R.S., Taylor, R. Intermolecular nonbonded contact distances in organic crystal structures: comparison with distances expected from van der Waals radii. *J Phys Chem* **100**, 7384-7391 (1996).

[72] Smart, O.S., Neduvelil, J.G., Wang, X., Wallace, B.A., Sansom, M.S.P. HOLE: A program for the analysis of the pore dimensions of ion channel structural models. *J Mol Graph* **14**, 354-360 (1996).

[73] Kahm, M., Hasenbrink, G., Lichtenberg-Fraté, H., Ludwig, J., Kschischo M. Fitting Biological Growth Curves with R. *J Stat Softw* **33**, 1-21 (2010).

[74] Zwietering, M.H., Jongenburger, I., Rombouts, F.M., van't Riet, K. Modeling of the bacterial growth curve. *Appl Environ Microbiol* **56**, 1875-1881 (1990).

[75] Blumberg, A.A. Logistic growth rate functions. *J Theoret Biol* **21**, 42 (1968).

[76] Gompertz, B. On the nature of the function expressive of the law of human mortality, and on a new mode of determining the value of life contingencies. *Philos Trans R Soc London* **115**, 513-585 (1825).

[77] Zwietering, M.H., Jongenburger, I., Rombouts, F.M., van't Riet, K. Modeling of the Bacterial Growth Curve. *Appl Environ Microbiol* **56** 1875-1881 (1990).

[78] Richards, F.J. A flexible growth function for empirical use. *J Exp Bot* **10**, 290-300 (1959).

[79] E., Tjørve, Tjørve, K.M.C. A unified approach to the Richards-model family for use in growth analyses: Why we need only two model forms. *J Theor Biol* **267**, 417-425 (2010).

[80] Eisenberg, D., Weiss, R.M., Terwilliger, T.C., Wilcox, W. Hydrophobic moments and protein structure. *Faraday Symp Chem Soc* **17**, 109-120 (1982).

[81] Kapcha, L.H., Rossky, P.J. A simple atomic-level hydrophobicity scale reveals protein interfacial structure. *J Mol Biol* **426**, 484-498 (2014).

[82] Gromiha, M.M., Oobatake, M., Kono, H., Uedaira, H., Sarai, H. Role of structural and sequence information in the prediction of protein stability changes: comparison between buried and partially buried mutations. *Protein Eng* **12**, 549-555 (1999).

[83] Gromiha, M.M. Factors influencing the thermal stability of buried protein mutants. *Polymer* **44**, 4061-4066 (2003).

[84] Robin, X., Turck, N., Hainard, A., Tiberti, N., Lisacek, F., Sanchez, J., Müller, M. pROC: an open-source package for R and S+ to analyze and compare ROC curves. *BMC Bioinformatics*, **12**, 77 (2011).

[85] Following [66], let us consider the case of a missense SCN9A mutation expressed in the perturbation form of $N(\mathbf{p}_{crit.}, l_\alpha(\mathbf{p}_{crit.})) \rightarrow N(\mathbf{p}_{crit.}, l_\alpha(\mathbf{p}_{crit.})) + \epsilon(\mathbf{p}_{crit.}, l_\alpha(\mathbf{p}_{crit.}))$, with $\epsilon(\mathbf{p}_{crit.}, l_\alpha(\mathbf{p}_{crit.})$ being a small-amplitude perturbation source describing addition and/or removal of a small number of atoms due mutation translation. Then, HIcIS is regulated according to $h_z^{(1)}(\mathbf{p}_{crit.}, l_\alpha(\mathbf{p}_{crit.})) + \zeta(\mathbf{p}_{crit.}, l_\alpha(\mathbf{p}_{crit.})) \sim l_\alpha(\mathbf{p}_{crit.})^{\gamma(\mathbf{p}_{crit.})} \cdot \big(N(\mathbf{p}_{crit.}, l_\alpha(\mathbf{p}_{crit.})) + \epsilon(\mathbf{p}_{crit.}, l_\alpha(\mathbf{p}_{crit.})\big)$ with $\gamma(\mathbf{p}_{crit.}) = \gamma_{partI}(\mathbf{p}_{crit.})$ for $s(\mathbf{p}_{crit.}) < l_\alpha(\mathbf{p}_{crit.}) \leq \xi(\mathbf{p}_{crit.})$ and $\gamma(\mathbf{p}_{crit.}) = \gamma_{partII}(\mathbf{p}_{crit.})$ for $\xi(\mathbf{p}_{crit.}) < l_\alpha(\mathbf{p}_{crit.}) \leq o(\mathbf{p}_{crit.})$ so that the HIIS law described by r1 remains intact around the critical point.

[86] Heyne, H.O., Baez-Nieto, Iqba, S. et al. A machine learning method can predict loss- versus gain-of-function effects of human genetic variants in disease-associated ion channels. *Sci Transl Med* **12**, 556 (2020).

[87] Tsuchiya, M., Giuliani, A., Hashimoto, M., Erenpreisa, J., Yoshikawa, K. Self-Organizing Global Gene Expression Regulated through Criticality: Mechanism of the Cell-Fate Change. *PLoSONE* **11**, 12 (2016).

[88] Pavlos, G.P., Karakatsanis, L.P., Iliopoulos, A.C. et al. Measuring complexity, nonextensivity and chaos in the DNA sequence of the Major Histocompatibility Complex. *Physica A* **438**, 188-209 (2015).

[89] Furusawa, C., Kaneko, K. Adaptation to optimal cell growth through self-organized criticality. *Phys. Rev. Lett.* **108**, 208103 (2012).

[90] Janina, H., Gross, T. Self-organized criticality as a fundamental property of neural systems. *Front Syst Neurosci* **8**, 166 (2014).

[91] Beggs, J.M. The criticality hypothesis: How local cortical networks might optimize information processing. *Phil Trans R Soc A* **366**, 329-343 (2008).

[92] Bertschinger, N., Natschlager, T. Real-time computation at the edge of chaos in recurrent neural networks. *Neural Comput* **16**, 1413-1436 (2004).

[93] Kinouchi, O., Copelli, M. Optimal dynamical range of excitable networks at criticality. *Nat Phys* **2**, 348-351 (2006).

[94] Watkins, N.W., Pruessner, G., Chapman, S.C. et al. 25 Years of Self-organized Criticality: Concepts and Controversies. *Space Sci Rev* **198**, 3-44 (2016).

[95] Shen, H., Liu, D., Wu, K., Lei, J., Yan, N. Structures of human $Na_V1.7$ channel in complex with auxiliary subunits and animal toxins. *Science* **363**, 1303-1308 (2019).

[96] Karczewski, K.J., Francioli, L.C., Tiao, G. et al. Variation across 141,456 human exomes and genomes reveals the spectrum of loss-of-function intolerance across human protein-coding genes. *bioRxiv*, 531210 (2019).

[97] Toffano, A., Chiarot, G., Zamuner, S. et al. Computational Pipeline to probe NaV1.7 gain-of-functions variants in neuropathic painful syndromes. *Sci Rep* **10**, 17930 (2020).